Supporting Information: Complete mapping of the thermoelectric properties of a single molecule

Pascal Gehring,* Jakub K. Sowa, Chunwei Hsu, Joeri de Bruijckere, Martijn van der Star, Jennifer J. Le Roy, Lapo Bogani, Erik M. Gauger, and Herre S.J. van der Zant

1. SHIFT OF CONDUCTANCE PEAK

For a weakly coupled molecule with large charging energy $\Gamma \ll k_{\mathrm{B}}T \ll e^2/C$ and a doubly degenerate ground state the conductance is given by:[1]

$$G = \frac{e^2}{h}\frac{1}{k_{\mathrm{B}}T}\frac{\Gamma_L\Gamma_R}{\Gamma_L+\Gamma_R}[1-f(\epsilon)]f(\epsilon - T\mathcal{S}_N + T\mathcal{S}_{N-1}) \tag{S1}$$

where $f(\epsilon)$ is the Fermi-Dirac distribution, and $\mathcal{S}_N$ and $\mathcal{S}_{N-1}$ are the entropies of the molecular quantum dot occupied with N and $N-1$ electrons, respectively. To derive this expression, the following assumptions were made. (1) The tunnel couplings of the two degenerate ground states with energy $E_1 = E_2 \equiv E$ to the leads are equal $\Gamma^{(1)}_{(L,R)} = \Gamma^{(2)}_{(L,R)} \equiv$

* pascal.gehring@uclouvain.be

$\Gamma_{(L,R)}$. (2) Each of the two ground states is occupied with the same probability. The shift of the conductance peak $\Delta\mu$ with temperature can be found by finding the maximum of Equation (S1):

$$\frac{\mathrm{d}G}{\mathrm{d}\epsilon} = k_{\mathrm{B}}T\exp(A)[f(A)]^2 f(A+B) + [1-f(A)][-k_{\mathrm{B}}T\exp(A+B)[f(A+B)]^2] = 0 \ , \tag{S2}$$

where $A = \epsilon/(k_{\mathrm{B}}T)$ and $B = (-T\mathcal{S}_N + T\mathcal{S}_{N-1})/(k_{\mathrm{B}}T)$.
Solving Equation (S2) yields the shift of the conductance peak

$$\Delta\mu(T) = \frac{1}{2}T\Delta\mathcal{S}, \tag{S3}$$

where $\mathcal{S}_N - \mathcal{S}_{N-1}$ is the difference in entropy between the N and $N-1$ charge ground states. Thus, the position of the conductance peak changes linearly with temperature with a slope given by the change in entropy of the molecule when one extra electron is added. If, for example, the molecule in the $N-1$ charge state is occupied by zero unpaired electrons (singlet ground state) and in the N charge state by one unpaired electron (doublet ground state) the entropy change upon adding one electron is given by

$$\Delta\mathcal{S} = \mathcal{S}_N - \mathcal{S}_{N-1} = k_{\mathrm{B}}\ln(2) - k_{\mathrm{B}}\ln(1) = k_{\mathrm{B}}\ln(2) \ . \tag{S4}$$

2. RATE-EQUATION MODEL

As discussed in the main body of this work, the charge transport through the molecular junction is modelled using the rate-equation-type approach from Ref. [2]. For clarity, we reiterate it below.

In the $\mathrm{RE}^{\mathrm{full}}$ model, the overall electrical current across the junction is given using the generic expression ($\hbar = 1$ throughout this section):

$$I_{\mathrm{sd}} = e\frac{\gamma_L\bar{\gamma}_R - \gamma_R\bar{\gamma}_L}{\gamma_L + \bar{\gamma}_L + \gamma_R + \bar{\gamma}_R} \ , \tag{S5}$$

where e is the electron charge, and γ_l and $\bar{\gamma}_l$ are the electron hopping rates for hopping on and off the molecular structure at the $l = L, R$ interface, respectively,

$$\gamma_l = d_N\Gamma_l\int\frac{\mathrm{d}\epsilon}{2\pi}f_l(\epsilon)k_+(\epsilon) \ ; \tag{S6}$$

$$\bar{\gamma}_l = d_{N-1}\Gamma_l\int\frac{\mathrm{d}\epsilon}{2\pi}[1-f_l(\epsilon)]k_-(\epsilon) \ . \tag{S7}$$

In the above, Γ_l is the molecule-lead coupling [such that $\Gamma = (\Gamma_L + \Gamma_R)/2$ is the lifetime broadening], d_N and d_{N-1} denote the degeneracies of the N and $N-1$ charge states (in the present case $d_N = 1$ and $d_{N-1} = 2$), and

$$k_\pm(\epsilon) = 2\,\mathrm{Re}\int_0^\infty \mathrm{d}\tau\, e^{\pm\mathrm{i}(\epsilon-\mu)\tau}e^{-\Gamma\tau}B(\tau) \ . \tag{S8}$$

In the above, μ is the position of the molecular energy level and $B(\tau)$ is the phononic correlation function. The single set of roughly equidistant peaks observed in the conductance maps (Figures 2, and Supplementary Fig.2 and 4) suggest that the electronic degrees of freedom are predominantly coupled to a single low-frequency vibrational mode of frequency ω[3]. Assuming that this mode is thermalized at all times, we have:[2, 4]

$$B(\tau) = \exp\left(\frac{g^2}{\omega^2}[\coth(\beta\omega/2)(\cos\omega\tau - 1) - \mathrm{i}\sin\omega\tau]\right) \ , \tag{S9}$$

where g is the electron-vibrational coupling strength,and β is the inverse phononic temperature, $\beta = 1/k_{\mathrm{B}}T_{ph}$.

Ignoring the electron-vibrational coupling amounts to setting $g = 0$, and therefore $B(\tau) = 1$. Then,

$$\gamma_l = d_N\Gamma_l\int\frac{\mathrm{d}\epsilon}{2\pi}f_l(\epsilon)\frac{2\Gamma}{(\epsilon-\mu)^2+\Gamma^2} \ ; \tag{S10}$$

$$\bar{\gamma}_l = d_{N-1}\Gamma_l\int\frac{\mathrm{d}\epsilon}{2\pi}[1-f_l(\epsilon)]\frac{2\Gamma}{(\epsilon-\mu)^2+\Gamma^2} \ . \tag{S11}$$

Supplementary Table. I. Parameters extracted from the various fits.

	RE (with vib. coupling)	RE (without vib. coupling)	Landauer-Büttiker
Γ_L	0.5 meV	1.52 meV	1.47 meV
Γ_R	84 μeV	10 μeV	50 μeV
Prefactor	3.275×10^{-4}	2.552×10^{-4}	6.309×10^{-4}
ω	1.8 meV	–	–
g/ω	0.86	–	–
T_L	3.50 K	2.86 K	2.86 K
T_R	2.68 K	2.00 K	2.00 K

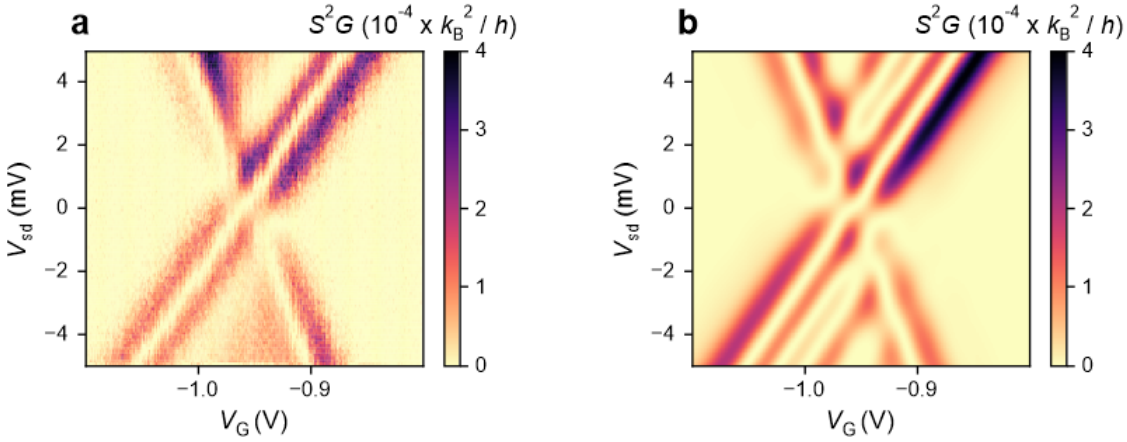

Supplementary Fig. 1. (a) Experimental and, (b) theoretical power factor as a function of the gate and bias voltage fro device **A**.

This constitutes the $\mathrm{RE}^{\mathrm{no-vib}}$ approach also discussed in the main body of this work.

Finally, in order to obtain the Landauer expression for the electric current, we further set $d_N = d_{N-1} = 1$. Then, the expression for current simplifies to

$$I = e \int \mathrm{d}\epsilon [f_L(\epsilon) - f_R(\epsilon)] \frac{\Gamma_L \Gamma_R}{\Gamma^2 + (\epsilon - \mu)^2} \ . \tag{S12}$$

3. FITS OF THE IV CHARACTERISTICS OF DEVICE A

As shown in the main body of this work, we fitted the IV characteristics on resonance using the three theoretical models outlined above (the rate-equation model with and without vibrational coupling, and the single-level Landauer-Büttiker approach).

The parameters obtained from these fits are listed in Table I.

Since we are considering experimental data only within a very small bias window, it is necessary to include an additional prefactor in the expression for the electric current. This prefactor accounts essentially for the ground-state-to-ground-state Franck-Condon factor for all the higher molecular vibrational modes (which cannot be excited within the considered bias window). The values of the prefactor and Γ_R (which is orders of magnitude smaller than Γ_L) cannot be completely separated since it is only their product that determines the magnitude of the electric current. This, however, does not change any of the underlying physics. The position of the molecular energy level can be inferred from the zero-bias thermocurrent measurements and is such that $\mu = 0$ at $V_G = -0.958$ eV. In the thermo-current calculations, we have kept the phononic temperature constant (at the base temperature of 2 K) as small variations of T_{ph} have little effect on the overall charge transport behaviour.

Finally, we can compare the experimental and theoretical power factors (as a function of the gate and bias voltage (the theoretical power factor was calculated using the parameters extracted from the IV fit and using the temperature difference extracted from the thermocurrent fit). They are shown in Supplementary Fig. 1 and are in a relatively good agreement.

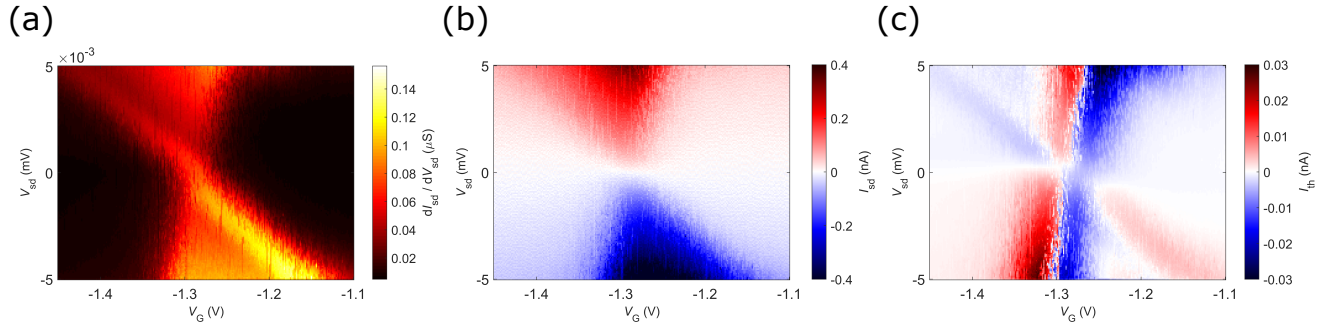

Supplementary Fig. 2. Experimental measurements for device **B**. (a) Map of differential conductance. (b) Stability diagram. (c) Map of thermocurrent.

Supplementary Table. II. Parameters extracted for device **B**.

Γ_L	Γ_R	T_L	T_R
0.36 μeV	0.83 meV	2.63 K (2 K)	K 3.60 K (3.03 K)

4. DEVICE B

We also consider another device, device **B**. Since we have demonstrated the importance of electronic degeneracies above, we will describe this device using a rate equation model discussed above. Furthermore, due to relatively noisy experimental signal together with considerable lifetime broadening, we are not able to resolve the effects of electron-vibrational coupling. We will therefore disregard the vibrational coupling in the modelling of this device (which as we shall see below will limit the applicability of the theoretical treatment to low bias potentials). The experimental conductance map, stability diagram and map of thermocurrent are shown in Supplementary Fig. 2.

First, from the thermocurrent measurement we extract the position of the molecular energy level which is $\mu = 0$ at $V_G = -1.294$ eV. We then fit the gate trace (zero-bias conductance) to extract the left and right molecule-electrode couplings, see Table II and Supplementary Fig. 3. Returning to the thermocurrent measurements, we then use the parameters extracted from the zero-bias conductance fit to determine the temperatures of the metallic leads during the thermocurrent measurements. We perform two fittings: one in which the temperature of the cold lead is kept at base temperature (2 K) and one in which both T_L and T_R are free fitting parameters. The results of both of these fits are shown in Supplementary Table II and Supplementary Fig. 3, and predict very similar temperature bias across the junction, $\Delta T \sim 1$ K. Both fits capture the asymmetry of the thermocurrent relatively well.

5. DEVICES C AND D

Below, in Supplementary Fig. 4, we further show the data for the devices **C** and **D**. Importantly, the conductance maps of both of these devices exhibit a low-lying (vibrational) excited state lines corresponding to the energies of 2.3±0.3 meV for device **C**, and 2.1±0.2 meV for device **D**. We have further performed a thermoelectric characterisation

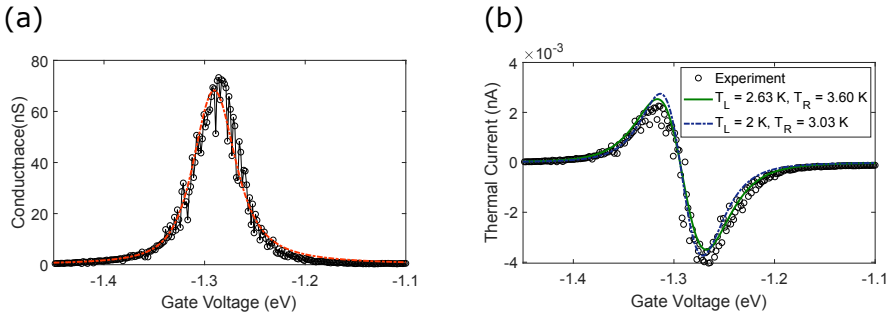

Supplementary Fig. 3. (a) Experimental and fitted zero-bias conductance. (b) Experimental and fitted thermocurrent at zero bias.

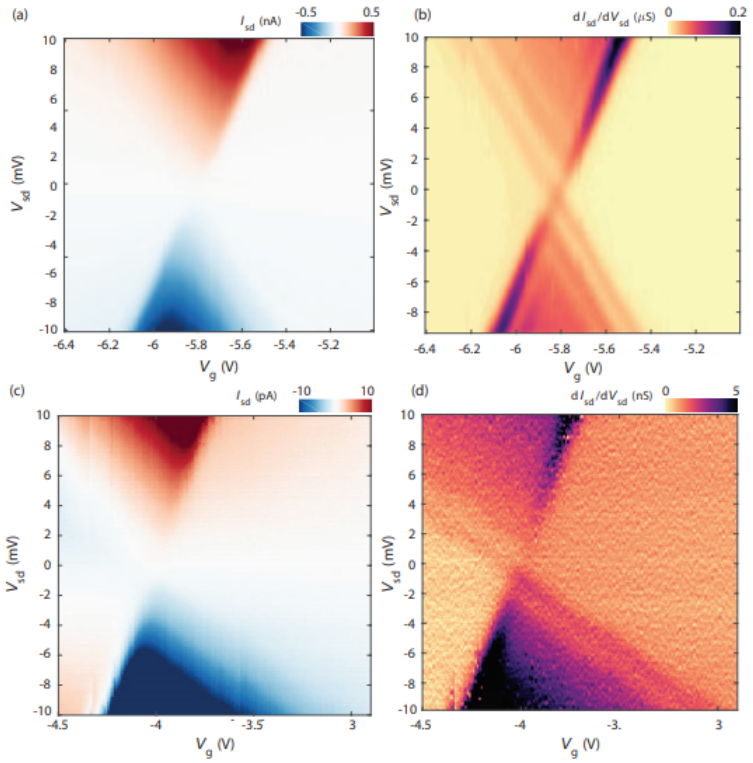

Supplementary Fig. 4. Experimental stability diagrams (a,c) and conductance maps (b,d) for devices **C** (a,b) and **D** (c,d).

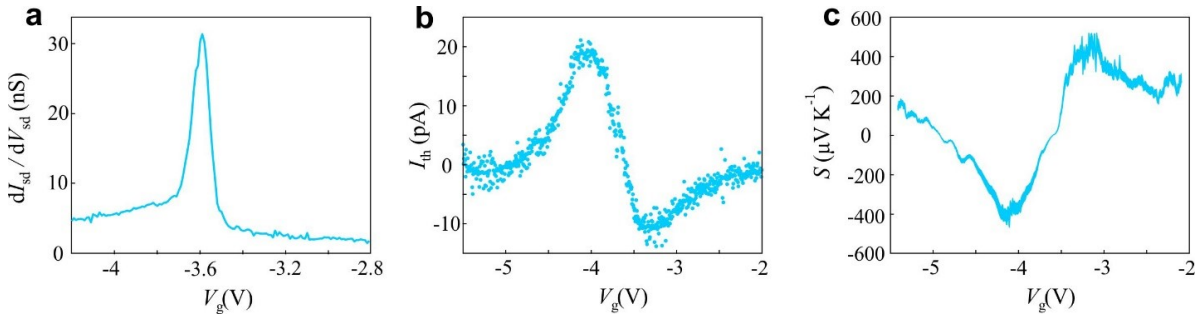

Supplementary Fig. 5. Experimental zero-bias conductance (a), thermocurrent (b) and estimated Seebeck coefficient (c) for device **C**.

of device **D**, as shown in Supplementary Fig. 5.

6. SYNTHESIS OF [GD(TPY-SH)$_2$(NCS)$_3$]

[Gd(tpy-SH)$_2$(NCS)$_3$] (see Supplementary Fig. 6 for its chemical structure) was synthesis using an analogous procedure to [Pr(tpy)$_2$(NCS)$_3$][5]. In this instance $Pr(NO_3)_3 \cdot 6H_2O$ was substituted of for $Gd(NO_3)_3 \cdot 6H_2O$ and typ was substituted for tpy-SH (typ = terpyridine).

7. DEVICE FABRICATION AND CALIBRATION

The devices used for thermoelectric studies presented here (which enable efficient heating of single-molecule junctions at cryogenic temperatures) were fabricated using a method described in detail elsewhere[6]. To this end, a Pd sample heater (3 nm Ti/27 nm Pd) and Pd gate electrode (1 nm Ti/6 nm Pd) were patterned on a Si wafer with 817 nm

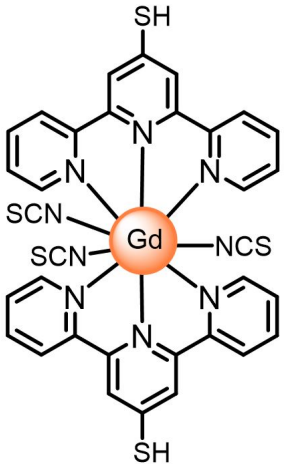

Supplementary Fig. 6. Chemical structure of $Gd(tpy\text{-}SH)_2(NCS)_3]$.

SiO_2 using standard electron beam lithography and electron beam evaporation. In a second step a 10 nm thick Al_2O_3 layer is deposited by atomic layer deposition, which serves as a gate dielectric and as an insulation layer to electrically insulate the sample heater from the drain and source leads.[7] In a third step, a 12 nm thin bow-tie shaped Au bridge (narrowest part < 60 nm) is evaporated and electrically contacted by two four-terminal thermometers (5 nm Ti/65 nm Au).

Full details about the device calibration can be found in [6]. A summary of these findings is presented below. To estimate the temperature drop on the junction created by the microheater, we employed two calibration techniques: Scanning thermal microscope (SThM) mapping in high vacuum and resistance thermometer method using the drain and source contacts as thermometers. For the former, we used a home-built high vacuum SThM with commercially available (Anasys Instruments, AN-300) doped silicon probes which are geometrically similar to standard micromachined AFM probes. For the resistance thermometer method, we used the four contacts connecting the drain and source lead to first measure their 4-terminal resistance as a function of T_{bath} in a cryostat. Thereafter the sample temperature was held constant and the 4-terminal resistance of the drain and source leads were measured as a function of dissipated heater power. Combining of both measurement results allowed estimating T_{drain} and T_{source} as a function of heater power P_{heater}. Using these two approaches we find $\Delta T/P_{\mathrm{heater}}$ values of 9.8 ± 1.2 K mW^{-1} using SThM and 10.7 ± 0.8 K/mW using the resistance thermometer method for a sample temperature of 50 K. We further note, that the induced temperature drop on the junction is drastically enhanced[7] and becomes a non-linear function of the heater power at cryogenic temperatures below 10 K. Furthermore, in this temperature range the resistance R of the resistance thermometers starts to saturate and $\mathrm{d}R/\mathrm{d}T$, which is used for calibration, becomes very small and the error in estimating ΔT becomes big. Lastly, the calibration of the micro-heater yields only the global temperature drop over the whole device (including the metallic contacts). The exact temperature distribution – and crucially the local temperature in close vicinity to the molecule – is therefore unknown. Therefore, we estimate the temperature drop on the molecular junction from electrical data: conductance and thermocurrent features broaden with temperature. This can be modelled by a Fermi-Dirac distribution (see Eq. S7) which contains the electron temperatures of the cold and hot leads. To this end, we can use the ratio of the thermocurrent signals close to the Coulomb diamond edge with positive and negative slope (see main text) to estimate the temperatures of the metallic contacts in direct vicinity (left: T_{L}, right: T_{R}) of the single molecule. In our experiment we heat the left side of the device. If only the temperature on the left side of the device was increased to $T_{\mathrm{L}} = \Delta T + T_{\mathrm{base}}$ while the right side remained at $T_{\mathrm{R}} = T_{\mathrm{base}}$, a thermocurrent signal would only be expected when μ_{mol} is close to μ_{L}. This means that only the edge of the Coulomb diamond with positive slope (which corresponds to $\mu_{\mathrm{mol}} = \mu_{\mathrm{L}}$ in our experiment) should be visible in the thermocurrent map. The fact that the other edge is also visible in Fig. 2c (main text) indicates that the thermal bias applied to the single molecule also to some extent heats up the colder right contact. From a fit to our data (using the $\mathrm{RE}^{\mathrm{full}}$ approach, see below) we find a temperature difference of $\Delta T = 0.8$ K with $T_{\mathrm{R}} = 2.7$ K, $T_{\mathrm{L}} = 3.5$ K, i.e., T_{R} increases by 0.7 K.

8. STATISTICAL ANALYSIS OF THE THERMOCURRENT ASYMMETRY

We performed measurements of I_{th} as a function of gate voltage V_{G} for device A (Fig. 2 in main text) 33 times where we varied the thermal bias ΔT (see Supplementary Fig. 7), the sample temperature T (2 - 9 K), the measurement frequency ω_1 (1.3Hz - 3Hz) and the integration times of the lock-in amplifiers (the distribution of the extracted $-I_{\mathrm{th,min}}/I_{\mathrm{th,max}}$ is shown in Supplementary Fig. 8). None of these variations seemed to influence the ratio $-I_{\mathrm{th,min}}/I_{\mathrm{th,max}}$ whose statistical error is solely given by measurement noise. Using the mean value and the standard deviation of this data set we obtain $-I_{\mathrm{th,min}}/I_{\mathrm{th,max}} = 1.4 \pm 0.2$.

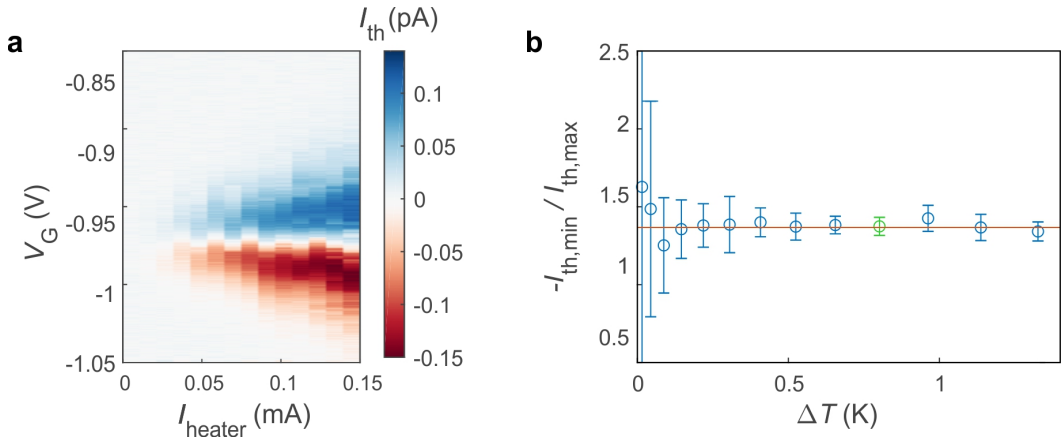

Supplementary Fig. 7. (a) Thermocurrent as a function of gate voltage and heater current for device **A**. (b) $-I_{\mathrm{th,min}}/I_{\mathrm{th,max}}$ as a function of heater current. The solid, orange line indicates the mean value of 1.4. The green data point indicates the temperature bias used in Fig. 2 and 3, main text.

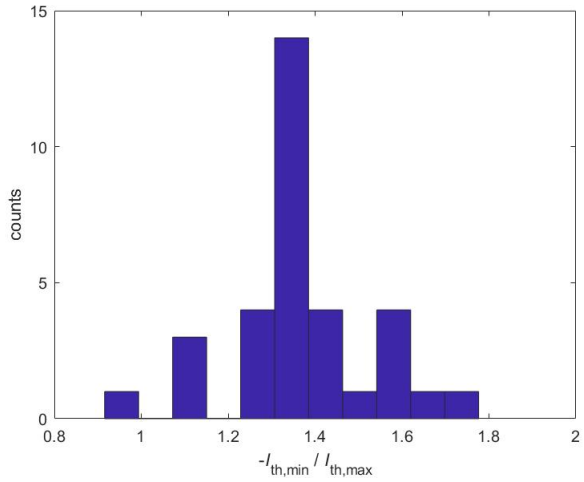

Supplementary Fig. 8. Distributions of the ratio $-I_{\mathrm{th,min}}/I_{\mathrm{th,max}}$ obtained from 33 single measurements under varying conditions.

9. DFT CALCULATIONS

In order to gain a deeper understanding of the role of the valance (4f) electrons in the electronic structure of the considered complex and the nature of the vibrational mode observed in our experimental study, we performed DFT calculations on the considered complex.

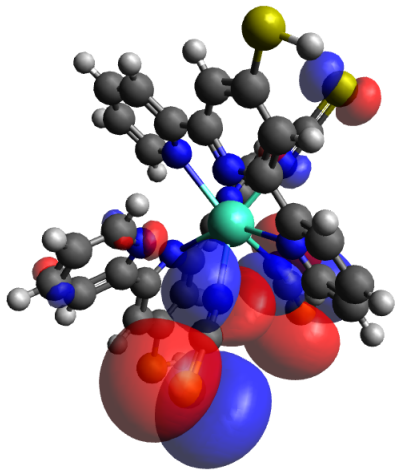

Supplementary Fig. 9. The calculated HOMO orbital (for spin alpha) for the considered molecular complex; iso-value of 0.01. See text for details.

Supplementary Table. III. The frequencies of the lowest molecular vibrational modes.

Vibrational mode	ω_1	ω_2	ω_3	ω_4	ω_5	ω_6	ω_7	ω_8	ω_9	ω_{10}
Frequency (meV)	1.32	1.58	2.28	2.35	2.85	2.98	3.00	3.96	4.58	4.83

9.1. HOMO orbital

The first set of calculations was performed in NWChem [8] using a B3LYP functional[9] and the small-core (28 electron) Stuttgart relativistic effective core potential (with the corresponding basis set) for the Gd atom and the 6-311G** basis set for light atoms. DFT calculations were performed assuming a multiplicity of 8 ($S = 7/2$; which corresponds to the most stable electronic configuration of the Gd^{3+} ion). Following the optimization of the complex (the output nuclear coordinates can be found in Section 14 14.1), the HOMO orbital is found at the energy of approximately -5.19 eV (*cf.* below). The 4f orbitals are buried over 5 eV below the energy of HOMO, and play little part in bonding. Furthermore, as shown in Supplementary Fig. 9, the HOMO orbital is localised largely on the (-SCN) ligands.

9.2. Vibrational analysis

The vibrational analysis was performed using Gaussian16.[10] We have once again used the B3LYP functional and 6-311G** basis set for light atoms. The Gd atom was described using the large core (53 electron; 4f electrons in the core) Stuttgart relativistic effective core potential (MWB53).[11, 12] Since the (unpaired) 4f electrons are captured within the large-core ecp, the structure was assumed to be a (pseudo-)singlet. [For the large-core ecp, the HOMO orbital is found at approx. -5.18 eV, *cf.* Section 9 9.1] The vibrational analysis was performed following the (gas phase) geometry optimization (the output nuclear coordinates can be found in Section 14 14.2). The frequencies of the 10 lowest vibrational modes are tabulated in Table III.

As can be seen above, the considered complex possesses a handful of low-frequency vibrational modes (although we note that the DFT calculations for such very low frequency modes can be somewhat unreliable and their frequencies can be expected to somewhat altered upon binding to the electrodes). We therefore conclude that the vibrational mode observed in our experiments is most likely of an intramolecular (rather than a "center-of-motion") character.

For the sake of completeness, Supplementary Fig. 10 shows the nuclear displacements associated with three of the lowest vibrational modes.

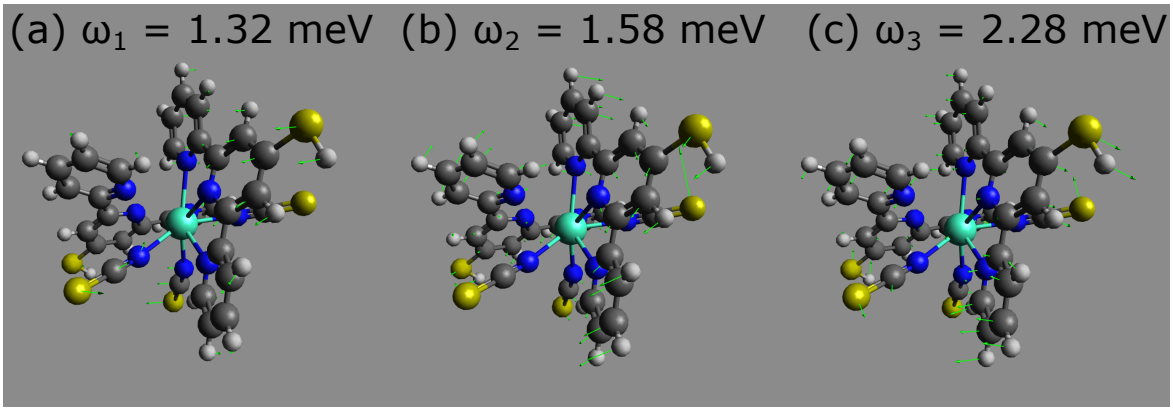

Supplementary Fig. 10. Nuclear displacements associated with three of the lowest molecular vibrational modes.

10. ELECTRONIC THERMAL CONDUCTANCE (RATE EQUATION)

The electronic thermal conductance, $\kappa_{\rm el}$, is given by

$$\kappa_{\rm el} = \frac{J_{\rm el}}{\Delta T}, \tag{S13}$$

where $J_{\rm el}$ is the electronic heat current induced by the thermal gradient ΔT. Considering the l interface, the heat current is given by[13–15]

$$J_{\rm el}^{(l)} = P_0 d_N \Gamma_l \int \frac{{\rm d}\epsilon}{2\pi}(\mu_l - \epsilon) f_l(\epsilon) k_+(\epsilon) + P_1 d_{N+1} \Gamma_l \int \frac{{\rm d}\epsilon}{2\pi}(\epsilon - \mu_l)[1 - f_l(\epsilon)] k_-(\epsilon) \ , \tag{S14}$$

where P_0 and P_1 are the populations of the states corresponding to the 'empty' and 'occupied' molecular level,

$$P_0 = \frac{\bar{\gamma}_L + \bar{\gamma}_R}{\gamma_L + \bar{\gamma}_L + \gamma_R + \bar{\gamma}_R} \ ; \tag{S15}$$

$$P_1 = \frac{\gamma_L + \gamma_R}{\gamma_L + \bar{\gamma}_L + \gamma_R + \bar{\gamma}_R} \ . \tag{S16}$$

Additionally, some of the energy is absorbed by the vibrational environment.[14] The relevant heat change rate is given by:

$$J_{(env)} = P_0 \sum_{l=L,R} \left\{ d_N \Gamma_l \int \frac{{\rm d}\epsilon}{2\pi}(\epsilon - \mu) f_l(\epsilon) k_+(\epsilon) \right\} + P_1 \sum_{l=L,R} \left\{ d_{N+1} \Gamma_l \int \frac{{\rm d}\epsilon}{2\pi}(\mu - \epsilon)[1 - f_l(\epsilon)] k_-(\epsilon) \right\} \ . \tag{S17}$$

As discussed in Ref. [14], the heat balance equation takes the form

$$J_{\rm el}^{(L)} + J_{\rm el}^{(R)} + J_{(env)} = (\mu_L - \mu_R) I/e \ , \tag{S18}$$

where I is the net current through the junction. In the case of zero-bias the above behaviour simplifies to,

$$J_{\rm el}^{(L)} + J_{\rm el}^{(R)} + J_{(env)} = 0 \ . \tag{S19}$$

Since the thermal conductance necessary to evaluate the figure of merit accounts for the rate at which the temperature gradient diminishes, here we will make use of the following value of the electronic heat current:

$$J_{\rm el} = \left(|J_{\rm el}^{(L)}| + |J_{\rm el}^{(R)}| \right) /2 \ . \tag{S20}$$

The electronic heat current will be evaluated using the parameters (including the temperature gradient) evaluated from the fit of the full rate equation approach in the limit of zero lifetime broadening, $\Gamma = 0$ (in order to avoid artefacts present for non-zero Γ). Since the zero-bias thermal current and the zero-bias conductance are generally overestimated around resonance when setting $\Gamma = 0$, we can expect that this approach will also overestimate the electronic heat conductance and consequently underestimate the figure of merit.

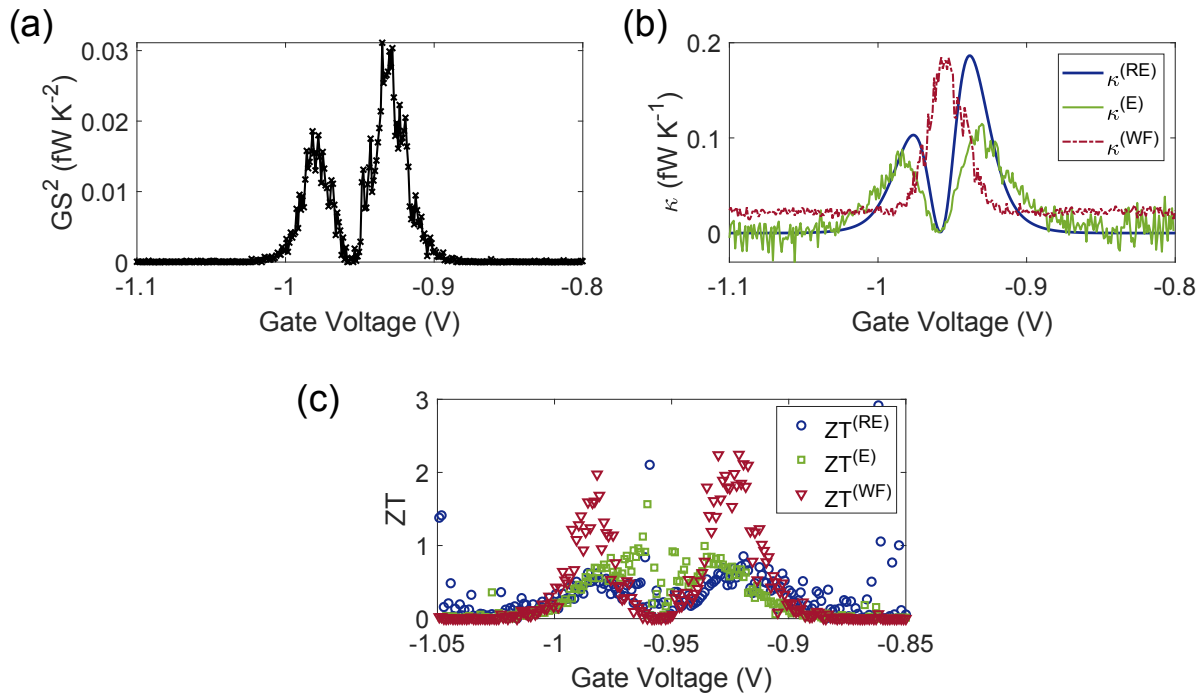

Supplementary Fig. 11. (a) Experimental GS^2 value at zero bias. (b) The value of the electronic heat conductance at zero bias calculated using different approaches. (c) The figure of merit obtained using the three different estimations of the electronic heat conductance ($V_{sd} = 0$).

11. FIGURE OF MERIT

In this section, we estimate the thermoelectric figure of merit for our device at zero bias. As discussed in the main body of this work, we will disregard the phononic heat conductance. The figure of merit, ZT, is therefore given by

$$ZT = \frac{GS^2 T}{\kappa_{\rm el}} \ . \tag{S21}$$

The power factor GS^2 is obtained from the experimental measurements of the thermal current and zero-bias conductance as

$$GS^2 = \left(I_{th}/\Delta T\right)^2 / G \ , \tag{S22}$$

where $\Delta T = 0.82$ K. The power factor (at zero bias as a function of gate voltage) is plotted in Supplementary Fig. 11(a).

The value of $\kappa_{\rm el}$ will be estimated here using three different methods.

1. (WF) Firstly, we will use the Wiedemann-Franz law which states that $\kappa_{\rm el}^{(WF)} = GLT$, where $L = 2.44 \times 10^{-8}$ W Ω K^{-2} is the Lorenz number and we take the temperature $T = (T_L + T_R)/2 = 3.09$ K.

2. (E) Secondly, we will use the approximate relation (exact in the absence of lifetime broadening/vibrational coupling) given by Esposito et al.[15] which states that $\kappa_{\rm el}^{(E)} = \mu I_{th}$, where I_{th} is the thermal current at zero bias and μ is the position of the molecular energy level relative to the Fermi energy of the unbiased leads.

3. (RE) Thirdly, we will use the rate equation approach, as outlined in Section 10. That is, we calculate the heat current $J_{\rm el}^{(L)}$ for zero bias and $T_L = 3.50$ K and $T_R = 2.68$ K. Then, $\kappa_{\rm el}^{(RE)} = J_{\rm el}^{(L)}/\Delta T$.

The values of $\kappa_{\rm el}$ obtained using these methods (again, at zero bias as a function of gate voltage) are plotted in Supplementary Fig. 11(b).

Finally, we use Eq. (S21) to estimate the figure of merit using the three aforementioned approaches. The values of ZT at zero bias (as a function of the gate voltage) are plotted in Supplementary Fig. 11(c). As stated in the main body of this work, the maximum values of ZT at zero bias are roughly $ZT_{max} \sim 2$ (Wiedemann-Franz law), $ZT_{max} \sim 1$ (approximate expression of Esposito et al.[15]), and $ZT_{max} \sim 0.7$ (rate equation model) [as can be seen in Supplementary Fig. 11(c), these are conservative estimates].

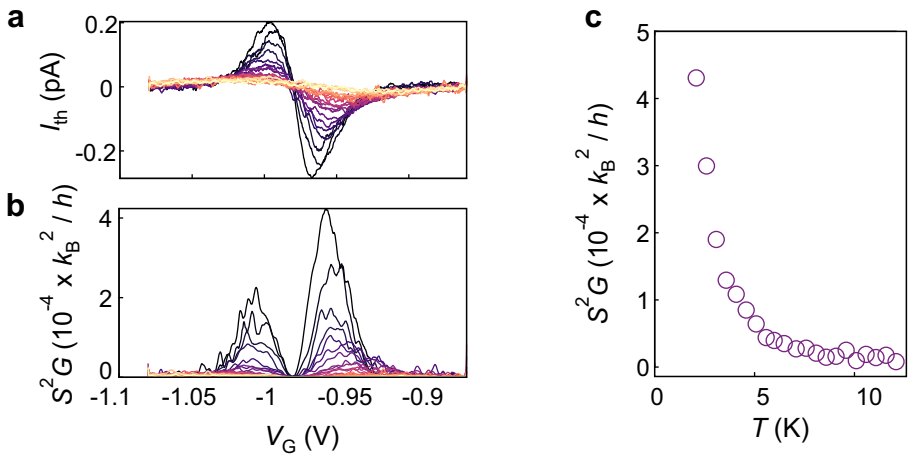

Supplementary Fig. 12. (a) Experimental thermocurrent $I_{\rm th}$ and (b) GS^2 gate-traces at zero bias at different temperatures (from 2 K (black) to 30 K (yellow)). (c) Maximum GS^2 as a function of temperature.

12. TEMPERATURE DEPENDENCE OF THE EXPERIMENTAL POWER FACTOR

13. ASYMMETRY OF I_{th} AND THE $I-V$ CHARACTERISTICS

As discussed in the main body of this work, we observe pronounced asymmetries in the $I-V$ characteristics on resonance as well as in the gate-dependent thermocurrent (at zero bias), see Fig. 3a and c in the main text.

First, in order to observe such pronounced asymmetry of the $I-V$ characteristics on resonance (Fig. 3a, main text), the system in question needs to simultaneously possess a (spin) degenerate energy level, exhibit strong electron-electron repulsion (which prevents doubly populating/emptying of the considered level), *and be asymmetrically coupled to the leads*. The reason for the asymmetry of the $I-V$ characteristics is that in the presence of strongly asymmetric coupling, the overall transport is limited by the interface with the weak molecule-lead coupling. Then, depending on the sign of the bias voltage, the overall current is determined by either the $N \to N-1$ or $N-1 \to N$ transition. Since the $N-1$ charge state is doubly degenerate, the former transition is twice as likely as the latter one. This leads to the observed asymmetry of the $I-V$ characteristics.

Second, we also observe the asymmetry of the zero-bias thermocurrent with respect to the gate voltage (around the charge degeneracy point, see Fig. 3c in the main text). In order to observe this asymmetry, *no asymmetric molecule-lead coupling* is necessary. The asymmetry instead results from the *two-fold degeneracy* of one of the charge states (together with strong electron-electron repulsion). For the thermocurrent the rate-limiting step is the electron transfer to and from the 'hot' contact. Depending on the value of $V_{\rm G}$, the electron transfer at the 'hot' interface corresponds either to a $N-1 \to N$ or to a $N \to N-1$ transition. Again, since the $N-1$ state is two-fold degenerate, the latter transition is more likely than the former, leading to the observed asymmetry of $I_{\rm th}$ which can therefore also be observed in the case of symmetric molecule-lead coupling. This is illustrated in Supplementary Fig. 13, which shows the calculated thermocurrent (at zero bias as a function of the gate voltage) for (a) symmetric molecule-lead coupling and non-degenerate electronic states; (b) asymmetric molecule-lead coupling and non-degenerate electronic states; and (c) symmetric molecule-lead coupling and two-fold degenerate $N-1$ state.

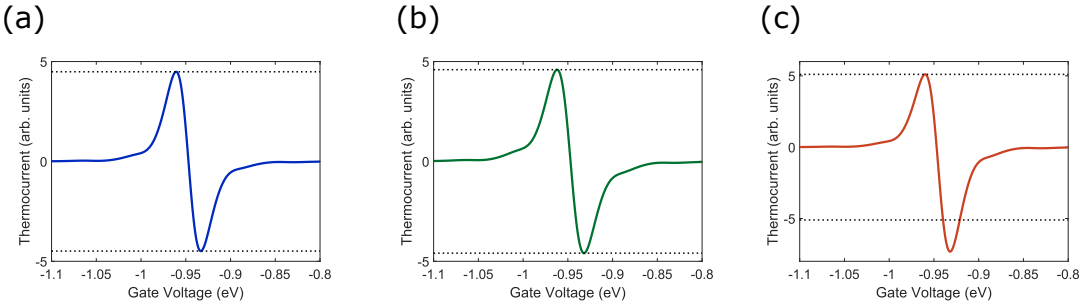

Supplementary Fig. 13. Thermocurrent calculated for (a) symmetric molecule-lead coupling ($\Gamma_L = \Gamma_R = 0.2$ meV) and non-degenerate electronic states; (b) asymmetric molecule-lead coupling ($\Gamma_L = 0.2$ meV and $\Gamma_R = 0.4$ meV) and non-degenerate electronic states; (c) symmetric molecule-lead coupling ($\Gamma_L = \Gamma_R = 0.2$ meV) and two-fold degenerate $N-1$ charge state. The dotted lines indicate $\max(I_{th})$ and $-\max(I_{th})$, and clearly indicate the asymmetry of thermocurrent in the case of (c). Other parameters similar to what was used before: $\omega_0 = 1.8$ meV, $g = 0.86\omega_0$, $T_L = 2.4$ K, $T_R = 3.3$ K, no prefactor was used and therefore the values of current are shown in arbitrary units.

14. NUCLEAR COORDINATES

14.1. Small core (28 electron) relativistic ECP/6-311G**/B3LYP

C 3.54951 -0.38226 -1.30055
C 1.23738 2.78849 2.25776
C 0.33840 -3.45380 -0.25638
C 2.32197 -1.72305 2.24925
H 2.88046 -1.67406 1.32335
C 2.72063 -2.54299 3.29917
H 3.61781 -3.14048 3.20395
C 1.92798 -2.59422 4.43847
H 2.18331 -3.24859 5.26363
C 0.79289 -1.79615 4.50374
H 0.15068 -1.83738 5.37300
C 0.48158 -0.96614 3.42255
C -0.66759 -0.02287 3.45933
C -1.16495 0.42413 4.68454
H -0.72059 0.07456 5.60508
C -2.18412 1.37072 4.70710
S -2.88055 2.03069 6.19486
C -2.66098 1.84811 3.48691
H -3.40011 2.63602 3.46751
C -2.12428 1.35185 2.30140
C -2.59246 1.88190 0.99046
C -3.82586 2.53191 0.86136
H -4.49210 2.62160 1.70789
C -4.20292 3.04424 -0.37230
H -5.15436 3.55038 -0.48562
C -3.34450 2.88790 -1.45359
H -3.59125 3.27129 -2.43538
C -2.15193 2.20351 -1.25275
H -1.46519 2.02730 -2.06975
C 1.53973 3.19662 -1.43421
H 1.33183 3.51314 -0.42044
C 2.23777 4.01116 -2.32191
H 2.56475 4.99397 -2.00743
C 2.50674 3.52717 -3.59482
H 3.05136 4.12708 -4.31430
C 2.06904 2.25222 -3.93492

H 2.25534 1.85787 -4.92433
C 1.37557 1.49747 -2.98832
C 0.84580 0.14120 -3.29272
C 1.35790 -0.63990 -4.32562
H 2.22521 -0.30958 -4.87874
C 0.77664 -1.88296 -4.58007
S 1.37214 -2.99331 -5.82282
C -0.33315 -2.27020 -3.82495
H -0.79126 -3.23639 -3.98368
C -0.77909 -1.43504 -2.80413
C -1.96091 -1.78113 -1.96777
C -2.94296 -2.66576 -2.42027
H -2.86891 -3.11221 -3.40239
C -4.02555 -2.95872 -1.60012
H -4.79264 -3.64818 -1.93193
C -4.09794 -2.35862 -0.35039
H -4.91403 -2.56314 0.33100
C -3.08380 -1.47876 0.01656
H -3.10185 -0.99845 0.98803
N 2.60995 -0.23548 -0.60113
N 1.06974 2.01225 1.38402
N 0.42667 -2.29051 -0.08717
N 1.22501 -0.95853 2.30449
N -1.14883 0.42256 2.28322
N -1.77915 1.70890 -0.06693
N 1.11135 1.97164 -1.75586
N -0.16901 -0.27267 -2.51431
N -2.04404 -1.18415 -0.76501
Gd 0.35702 0.11785 0.08790
S 4.81669 -0.57114 -2.30115
S 1.43478 3.86488 3.46063
S 0.17644 -5.05241 -0.51900
H -2.02605 1.43298 7.04755
H 2.51292 -2.32805 -6.08996

14.2. Large core (53 electron) relativistic ECP/6-311G**/B3LYP

C -2.46577 1.38962 -2.58233
C 2.55218 2.65102 -1.05363
C -1.43796 -2.92621 -1.30947
C 0.71830 -0.90817 -3.48308
H -0.26314 -0.45620 -3.55211
C 1.25490 -1.65279 -4.52764
H 0.69157 -1.77979 -5.44286
C 2.49869 -2.24432 -4.34928
H 2.93518 -2.86335 -5.12432
C 3.17739 -2.03666 -3.15492
H 4.13805 -2.50500 -2.98880
C 2.58899 -1.24124 -2.16742
C 3.29563 -0.90529 -0.90209
C 4.69039 -0.93277 -0.85553
H 5.25246 -1.21196 -1.73488
C 5.34624 -0.53132 0.30378
S 7.10774 -0.49727 0.47567
C 4.57013 -0.10266 1.37997
H 5.04839 0.28505 2.26785
C 3.18186 -0.10963 1.26853

C 2.34062 0.38876 2.39327
C 2.83733 0.47054 3.69974
H 3.83492 0.12545 3.93260
C 2.03057 0.98010 4.70786
H 2.40419 1.05017 5.72273
C 0.74037 1.38856 4.39286
H 0.07410 1.79505 5.14302
C 0.30920 1.24758 3.07945
H -0.69636 1.52172 2.78882
C -0.74618 3.75227 0.33133
H 0.32484 3.77112 0.17672
C -1.49559 4.92478 0.37910
H -1.00207 5.88336 0.28230
C -2.87111 4.82686 0.53782
H -3.49123 5.71481 0.57530
C -3.44721 3.56578 0.64273
H -4.51517 3.46342 0.77782
C -2.62785 2.43827 0.58434
C -3.17106 1.05974 0.71772
C -4.50401 0.76011 0.44939
H -5.16217 1.51838 0.05056
C -4.94827 -0.55069 0.63146
S -6.59829 -1.07152 0.26099
C -4.05289 -1.49757 1.13499
H -4.36082 -2.52578 1.26436
C -2.73427 -1.11876 1.37246
C -1.72826 -2.07436 1.91126
C -2.10932 -3.20166 2.64262
H -3.15337 -3.39604 2.84654
C -1.13185 -4.06764 3.11701
H -1.41004 -4.95116 3.67916
C 0.20021 -3.78279 2.84879
H 0.99801 -4.43395 3.18308
C 0.49376 -2.63013 2.12603
H 1.52121 -2.38003 1.88815
N -1.48771 0.99543 -2.04914
N 1.57189 2.03682 -0.81099
N -0.93982 -1.88227 -1.07435
N 1.36445 -0.71440 -2.32740
N 2.55002 -0.51391 0.14892
N 1.08090 0.75942 2.10183
N -1.29253 2.53658 0.43866
N -2.29265 0.12589 1.12239
N -0.43561 -1.78774 1.67259
Gd 0.00181 0.24111 -0.29550
S -3.82970 1.93840 -3.27343
S 3.91039 3.48897 -1.35847
S -2.13286 -4.36956 -1.59006
H 7.39708 -0.78538 -0.80801
H -6.96135 0.03823 -0.41130

[1] Beenakker, C. Theory of coulomb-blockade oscillations in the conductance of a quantum dot. *Phys. Rev. B* **44**, 1646 (1991).

[2] Sowa, J. K., Mol, J. A., Briggs, G. A. D. & Gauger, E. M. Beyond marcus theory and the landauer-büttiker approach in molecular junctions: A unified framework. *J. Chem. Phys.* **149**, 154112 (2018).

[3] Galperin, M., Ratner, M. A. & Nitzan, A. Molecular transport junctions: vibrational effects. *J. Condens. Matter Phys.* **19**, 103201 (2007).

[4] Electron transfer rates from time-dependent correlation functions. wavepacket dynamics, solvent effects, and applications. *J. Photochem. Photobiol. A* **82**, 87 – 101 (1994).

[5] Synthesis of complexes of 2,2:6,2-terpyridine and 1,10-phenanthroline with lanthanide thiocyanates; the molecular structures of [ln(terpy)2(ncs)3] (ln=pr, nd), [nd(terpy)2(ncs)3]·2etoh and [ln(phen)3(ncs)3]·etoh (ln=pr, nd). *Polyhedron* **22**, 1489 – 1497 (2003).

[6] Gehring, P. *et al.* Efficient heating of single-molecule junctions for thermoelectric studies at cryogenic temperatures. *Appl. Phys. Lett.* **115**, 073103 (2019).

[7] Gluschke, J. G., Fahlvik Svensson, S., Thelander, C. & Linke, H. Fully tunable, non-invasive thermal biasing of gated nanostructures suitable for low-temperature studies. *Nanotechnology* **25**, 385704 (2014).

[8] Apra, E. *et al.* Nwchem: Past, present, and future. *J. Chem. Phys.* **152**, 184102 (2020).

[9] Becke, A. D. Density-functional thermochemistry. iii. the role of exact exchange. *J. Chem. Phys.* **98**, 5648–5652 (1993).

[10] Frisch, M. *et al.* Gaussian 16 (2016).

[11] Dolg, M., Stoll, H., Savin, A. & Preuss, H. Energy-adjusted pseudopotentials for the rare earth elements. *Theor. Chim. Acta* **75**, 173–194 (1989).

[12] Dolg, M., Stoll, H. & Preuss, H. A combination of quasirelativistic pseudopotential and ligand field calculations for lanthanoid compounds. *Theor. Chim. Acta* **85**, 441–450 (1993).

[13] Craven, G. T. & Nitzan, A. Wiedemann–franz law for molecular hopping transport. *Nano Lett.* **20**, 989–993 (2020).

[14] Zimbovskaya, N. A. & Nitzan, A. Energy, work, entropy, and heat balance in marcus molecular junctions. *J. Phys. Chem. B* **124**, 2632–2642 (2020).

[15] Esposito, M., Lindenberg, K. & Van den Broeck, C. Thermoelectric efficiency at maximum power in a quantum dot. *EPL* **85**, 60010 (2009).